Lawrence Berkeley National Laboratory
Recent Work

Title
On the Conversion of Bauxite Ores to Highly Activated Alumina Media for Water Remediation

Permalink
https://escholarship.org/uc/item/4tr367p5

Journal
Advanced Sustainable Systems, 3(7)

ISSN
2366-7486

Authors
Haddad, AZ
Pilgrim, CD
Sawvel, AM
et al.

Publication Date
2019-07-01

DOI
10.1002/adsu.201900005

Peer reviewed

On the Conversion of Bauxite Ores to Highly Activated Alumina Media for Water Remediation

Andrew Z. Haddad,* Corey D. Pilgrim, April M. Sawvel, James Nathan Hohman, and Ashok J. Gadgil

Good quality drinking water is necessary to maintain a high quality of life. Millions lack access to clean and safe drinking water, and current trends suggest that billions will face acute water shortages in the coming decades. Development of new materials has led to technological impacts on water purification, from desalination membranes to atmospheric water scavenging. However, the most challenging aspect of technological solutions is cost: if the community being serviced cannot afford the solution, it is not likely to be sustainable. Repurposing Earth-abundant materials to replace highly engineered solutions is an atractive solution. Herein, minimal processing of bauxite rocks produces a high-porosity and reactive activated alumina in situ, without purification directly from the ore. This acid-treated, thermally activated bauxite (ATAB) exhibits a high surface area of 401 ± 6 m^2 g^{-1}, a 40-fold increase relative to its parent ore, and a 2× increase relative to the state-of-the-art fluoride adsorbent, activated alumina. The composition, preparation, and mechanism of adsorption are studied by X-ray diffraction, X-ray photoelectron spectroscopy, and multiple-quantum magic-angle spinning ^{27}Al nuclear magnetic resonance (NMR). The maximum adsorption density of ATAB is comparable with that of activated alumina, but ATAB requires fewer processing steps, thus warranting future consideration as a primary adsorbent of choice for fluoride removal from water.

Dr. A. Z. Haddad, Prof. A. J. Gadgil
Energy Technologies Area
Lawrence Berkeley National Laboratory
Berkeley, CA 94720, USA
E-mail: azhaddad@lbl.gov
Dr. C. D. Pilgrim
Department of Chemistry
University of California
Davis, CA 95616, USA
Dr. A. M. Sawvel
Materials Science Division
Lawrence Livermore National Laboratory
Livermore, CA 94550, USA
Dr. J. N. Hohman
The Molecular Foundry
Lawrence Berkeley National Laboratory
Berkeley, CA 94720, USA
Prof. A. J. Gadgil
Department of Civil and Environmental Engineering
University of California
Berkeley, CA 94720-1710, USA

The ORCID identification number(s) for the author(s) of this article can be found under https://doi.org/10.1002/adsu.201900005.

1. Introduction

Skeletal fluorosis is a debilitating condition endemic in 20 countries,[1–4] affecting an estimated 200 million people predominantly in rural, semi-arid regions of eastern Africa, southern Asia, and India.[5,6] It is a result of drinking water with high fluoride concentrations (>10 ppm) and most severely impacts children. Most fluoride contamination is naturally occurring, originating in groundwater from the minerals sellaite (MgF$_2$), fluorspar (CaF$_2$), cryolite (Na$_3$AlF$_6$), and fluorapatite (Ca$_5$(PO$_4$)$_3$F), among others.[7] Remediation is commonly achieved via reverse osmosis, or related technological solutions in developed countries, but energy-intensive industrial methods are often not sustainable in remote, resource-poor, or rural areas for reasons varying from the skilled labor requirements, lack of scalability, inherently high cost, or poor distribution networks. While the majority of groundwater fluoride contamination is due to natural causes, anthropogenic sources of fluoride are also prevalent. Fluoride forms a common aqueous effluent resultant in many chemical industries such as semiconductor, ceramic, glass, and metal-processing.[8–10] Excess fluorides from these effluents pose significant health hazards, and underscore the need for cost-effective industrial wastewater treatment methods.

Fluoride's chemical affinity for aluminum makes adsorption the most attractive option for remediation.[11] The current state-of-the-art adsorbent is activated alumina (AA), a refined aluminum product with porous γ-Al$_2$O$_3$ crystal structure.[12,13] Recently, we and others have explored the use of its precursor, bauxite ore, as an alternative adsorbent.[14–24] Bauxite is a globally abundant ore of aluminum and is vastly less expensive. Whereas AA is about \$2000 per ton, bauxite is less than \$40.[22,25] One advantage of activated alumina is its high porosity and surface area in excess of 200 m^2 g^{-1}.[12] Recently, we showed that treatment of raw Indian bauxite at 300 °C results in a 15-fold increase in specific surface area, from 11 to 170 m^2 g^{-1}.[23] Adsorption on this material was optimal at pH 6, and presumably the slightly acidic environment provides an enhanced attraction between hydroxyl sites on the bauxite surface and the anionic fluoride,[14] although there has been no systematic study of the coordination environment of the bound fluoride.

The enhancement of fluoride binding at mildly acidic conditions led us to test whether acid treatment of a thermally activated bauxite (TAB) might further enhance its adsorptive properties.[1–7,11,14–23,25–27] In this study, we demonstrate that a combined thermal and acid treatment effectively converts bauxite ore into a highly activated alumina. The resulting acid-tempered product is highly porous and exhibits fluoride adsorption capacities that are competitive with state-of-the-art industrial materials. This potentially low-cost treatment produces a high yield of boehmite, as demonstrated by powder X-ray diffraction (vide infra). We performed an investigation of the performance and mechanism of acid-treated, thermally activated bauxite (ATAB), including its synthetic preparation, material characterization, a detailed kinetic and thermodynamic analysis, isotherm analysis, and examination of aluminum coordination environments. Fluoride adsorption onto ATAB follows pseudo-second order kinetics and exhibits a maximum second order rate constant of 6.57×10^{-2} g mg^{-1} min^{-1} at 25 °C. The chemisorption of fluoride onto ATAB is exothermic, spontaneous, and exergonic with a $\Delta G°$ of −5.02 kJ mol^{-1} and a $\Delta H°$ of −41.6 kJ mol^{-1} at 25 °C using an initial fluoride concentration of 10 ppm.

2. Results and Discussion

Bauxite is a complex composite crystal comprised of various aluminum oxides, hydroxides, and additional compounds, and they are variable in their composition across the Earth.[28] **Scheme 1** shows the schematic overview of the conversion of bauxite to ATAB. This highly activated form of bauxite effectively scavenges fluoride from aqueous solution under mildly acidic conditions. In the following sections, we will discuss our characterization of the various synthetic and physical aspects of the transformation of raw bauxite to ATAB, and demonstrate its efficacy and absorption ability in later sections.

2.1. Overview of Chemical Formation of ATAB

Figure 1A shows the X-ray diffraction (XRD) pattern of TAB, as well as ATAB, where samples were made from the same TAB batch. ATAB is shown before and after fluoride adsorption. Both patterns of ATAB are indistinguishable from one another, displaying peaks at 22 and 34 2θ(°)-λ-$_{Co}$, assigned as boehmite. Other smaller peaks at 48 and 54 2θ(°)-λ-$_{Co}$ are indexed as hematite and anatase, respectively. The appearance of crystalline boehmite in ATAB XRD patterns is in stark contrast to the XRD pattern observed for TAB, which only shows crystalline features corresponding to hematite and anatase.[23]

The treatment of various aluminum oxides and hydroxides with 5 M HCl facilitates the formation of crystalline boehmite.[29] While crystalline phase changes are generally observed under either extreme heat or pressure exposures, crystalline transformations in highly acidic solutions or under acidic-hydrothermal conditions (temperatures ranging from 100 to 300 °C) have been observed previously in iron[30–34] and aluminum[29,35] compounds, and are attributed to dissolution, precipitation mechanisms. In the case of bauxite, the thermal treatment at 300 °C facilitates the transformation of the initial aluminum phase in bauxite, gibbsite, to boehmite,[35,36] via dehydroxylation of gibbsite (loss of water molecules, and was confirmed previously using thermogravimetric analysis-mass spectrometry (TGA-MS)).[23] Examination of Figure 1A reveals no crystalline boehmite in TAB, rather existing only in the amorphous phase. This is rationalized by the dehydroxlation process that occurs when exposed to temperatures of 300 °C, resulting in consecutive loss of water molecules from Al centers over extended periods of time; this prolonged exposure degrades the edge-site packing environment, removing the necessary hydroxyl groups, needed for the boehmite packing. The Gibbs–Curie–Wulff law[29] supports this claim, telling that linear crystal plane growth rates are proportional to the crystal surface energy densities. For boehmite, these surface energy densities are a direct consequence of the density of bound
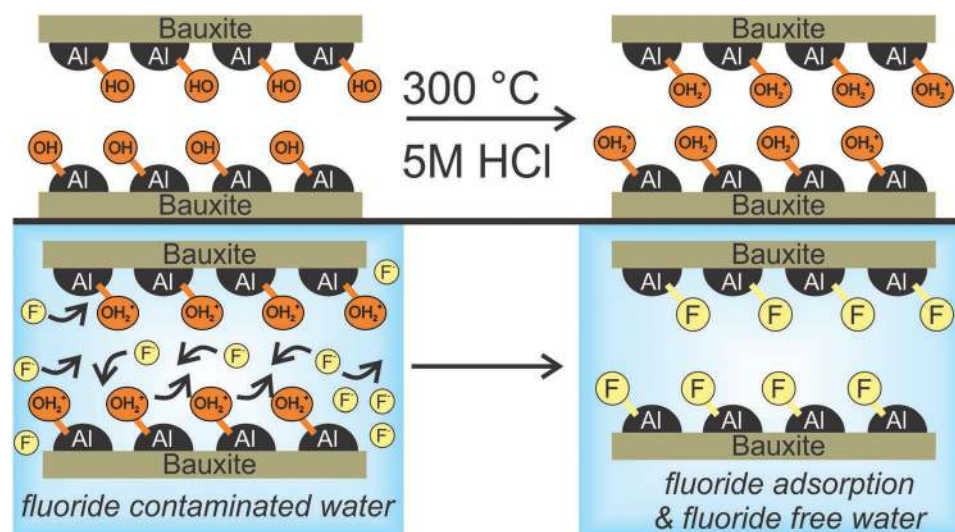
Scheme 1. Overview of the activation of crushed bauxite ore through heat and acid treatments, which converts bauxite into acid-treated thermally activated bauxite (ATAB). ATAB then readily adsorbs fluoride from aqueous solutions.
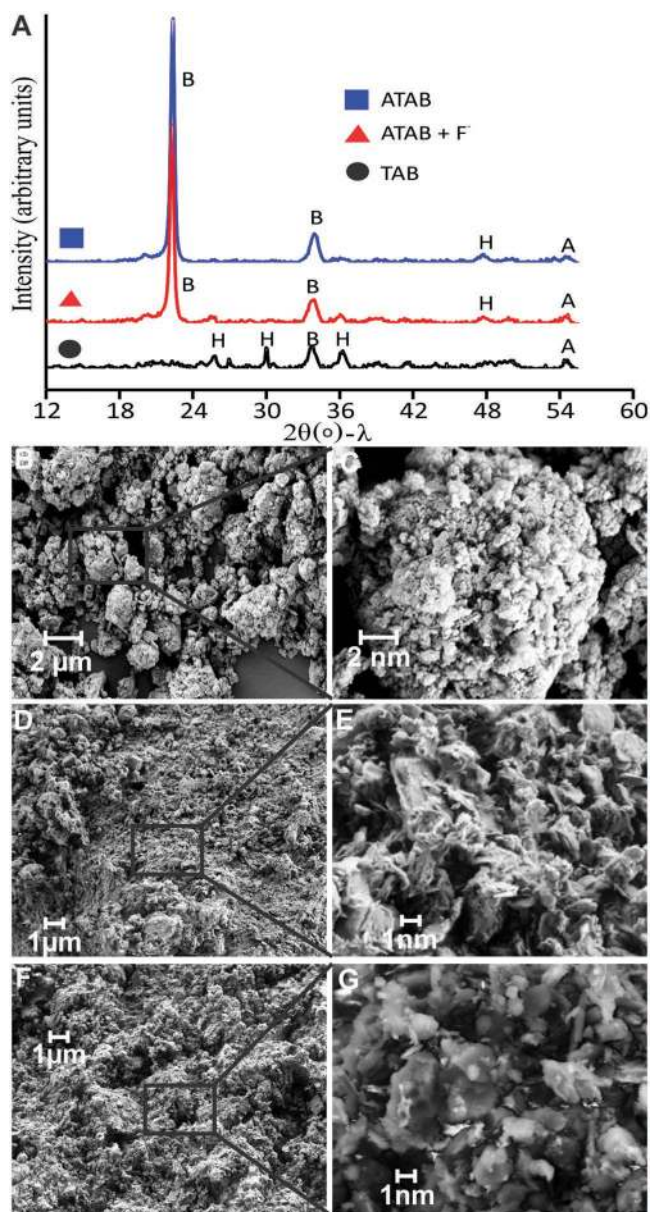
Figure 1. A) X-ray diffraction pattern of TAB (black), ATAB bauxite (blue), and ATAB bauxite after adsorption of fluoride (red). SEM images of TAB at B) 5 K magnification and C) 35 K magnification. SEM images of ATAB before fluoride adsorption at D) 5 K magnification and E) 35 K magnification. SEM images of ATAB + F⁻ at F) 5 K magnification and G) 35 K magnification.

surface hydroxyl groups. The treatment of TAB with a highly acidic solution, such as 5 M HCl, provides the necessary protons needed to generate the desired dense surface hydroxyl sites, existing as AlO(OH), or protonated boehmite, existing as $AlO(OH_2)^+$. Figure 1B–G shows scanning electron microscopy (SEM) images of TAB, ATAB, and ATAB after fluoride adsorption at magnifications of 5 and 35K, and give insight into the surface morphologies. The TAB, ATAB, and ATAB + F⁻ materials show similar morphology, however, Brunauer–Emmett–Teller (BET) results (Figure 3A; Figure S9, Supporting Information) show that porosity and BET surface area increases from 169

in TAB to 401 m² g⁻¹ in ATAB. Post fluoride adsorption, small morphological changes can be seen. We observe small crystallites appearing at a higher contrast in the high magnification SEM images post fluoride adsorption, Figure 1G. The crystallites are indicative of bound fluoride onto bauxite, and appear similar to light snow dusting on trees.

X-ray photoelectron spectroscopy (XPS) was performed on ATAB bauxite, before and after fluoride adsorption, for elemental analysis and examination of aluminum phases (Figures S1–S4, Supporting Information). **Table 1** shows the atomic percent changes before and after fluoride adsorption. The adsorption of fluoride results in an increase in fluorine percentage change in the F1s spectra increasing from 0.25 to 2.76%. This increase is concurrent with a decrease in oxygen percent, moving from 64.6 to 60.4%, supporting a ligand exchange mechanism implicating hydroxyl and fluoride exchange. Comparison of the major metal contributions in ATAB and the previously reported TAB[22] shows a significant decrease in the iron, titanium, and aluminum percent compositions, Figure S5 (Supporting Information), attributed to dissolution of mineral sources of these elements with 5 M HCl. This is consistent with many reports in literature suggesting that acid treatment of bauxite or red clays removes iron and titanium oxides, improves crystallinity, and increases surface area.[37,38] In line with these reports, specific surface area of ATAB increases to 401 ± 6 m² g⁻¹ after treatment with 5 M HCl, a 2.5× increase when compared to previously reported TAB,[23] and a 40× increase relative to its parent ore.

²⁷Al magic angle spinning nuclear magnetic resonance (MAS-NMR) provides a better understanding of the aluminum coordination environment in ATAB. Analysis was performed using a 14.1T magnet with v_R at 50 kHz. Two peaks are present at 70 and 8 ppm indicative of tetrahedral and octahedral coordination environments,[39] respectively, as seen in **Figure 2**. Integration of both peaks gives 12.1% tetrahedral and 87.9% octahedral. The peak at 70 ppm is consistent with tetra-coordinate γ-alumina, while the peak at 8 ppm is indicative of hexa-coordinate boehmite.[40] ATAB samples exposed to solutions of 10 ppm fluoride were subsequently examined and yielded similar results, again demonstrating peaks at 70 and 8 ppm, again, indicative of tetra-coordinate γ-alumina and hexa-coordinate boehmite, respectively.[40] Integration yields values of 12.3% tetrahedral and 87.7% octahedral (Figure 2, bottom trace), suggesting that the aluminum coordination environments undergo minimal structural changes during adsorption. To rule out any hidden 5-coordinate aluminum species, multiple-quantum magic-angle spinning (MQMAS) ²⁷Al was performed. Overlays indicate that only the two isotropic peaks at 70 and 8 ppm are observed, Figure S6 (Supporting Information), confirming only two coordination sites of aluminum in ATAB.

Further examination of high-resolution Al2p XPS spectra of ATAB before and after fluoride adsorption provides additional information about the identity of the aluminum and fluorine coordination compounds, **Figure 3**A. Prior to fluoride adsorption, Al2p spectra show a broad asymmetric band, centered at 75 eV; fit to two bands with binding energies at 74.39 and 75.57 eV, corresponding to octahedral boehmite and tetrahedral aluminum oxide.[41,42] The band corresponding to boehmite at 74.39 eV after integration corresponds to 87.5% of the Al2p band, while the band assigned to γ-alumina represents 12.5%.

Table 1. Elemental analysis from high resolution XPS of ATAB bauxite before and after fluoride adsorption.

	ATAB at%						
Element	Carbon	Oxygen	Fluorine	Aluminum	Silicon	Titanium	Iron
% (before F⁻ adsorption)	10.5 ± 0.4	65.6 ± 1	0.25 ± 0.15	14.8 ± 0.35	6.8 ± 0.5	0.4 ± 0.1	2.5 ± 0.2
% (after F⁻ adsorption)	10.5 ± 1.15	60.4 ± 1.77	2.76 ± 0.26	14.4 ± 1.20	6.8 ± 1.74	0.4 ± 0.1	2.57 ± 0.1

These values agree within one percent with the integration percentages for tetrahedral and octahedral aluminum species obtained via ^{27}Al MAS-NMR. While XPS only assesses surface composition, NMR probes the bulk structure. The excellent agreement between XPS and NMR data confirms that the elemental composition measured at the surface by XPS is representative of the elemental composition and Al coordination throughout the entire sample.

After exposure to 10 ppm fluoride, Al2p spectra again demonstrate a broad asymmetric band, centered at ≈74 eV, Figure 3B. Two bands can be fit with binding energies at 74.39 and 75.57 eV, corresponding to octahedral boehmite and tetrahedral γ-alumina. The band corresponding to boehmite at 74.39 eV integrates to 86.7%, while the peak assigned to aluminum oxide represents 13.3%, consistent within one percent of the integration values for tetrahedral and octahedral aluminum species obtained via ^{27}Al MAS-NMR post fluoride adsorption. Based on strong literature precedent, coordination of the fluoride ions occurs at the six-coordinate boehmite aluminum species via ligand exchange between hydroxyl groups and fluoride anions.[22,23,43] However, further work including 2D ^{27}Al and ^{19}F correlation NMR experiments must be performed for confirmation, and to exclude any other potential aluminum coordination environments. These experiments are currently underway in our laboratory.

2.2. Adsorption Isotherms and Effect of Adsorbent Dose

Figure 3A shows the relationship between adsorption density and equilibrium solute concentration for ATAB, TAB, and raw bauxite using a dosage of 1 g L^{-1}. ATAB shows adsorption densities higher than our previously reported bauxites,[22,23] while also being competitive with reported values for activated alumina.[44] The ATAB isotherm was fitted using ISOFIT[45] as a Langmuir–linear partition (LLP) model, a dual-mode formulation that incorporates both Langmuir and linear isotherm behavior. The LLP model is described by Equation (1), where q is the adsorption density (mg g^{-1}), Q_0 is the calculated maximum adsorption density (mg g^{-1}), C_i is the equilibrium fluoride concentration (mg L^{-1}), b is a constant describing the affinity of the adsorbent to the adsorbate (L mg^{-1}), and k_p is a linear partitioning parameter constant (L mg^{-1})[46]

$$q = \frac{Q_0 b C_i}{1 + b C_i} + k_p C_i \tag{1}$$

Table 2 provides an overview of the values obtained from the fit of the LLP isotherm model. The model affords a value of Q_0, the calculated maximum adsorption density of 7.47 mg g^{-1}. This is comparable to AA, which shows a Q_0 of 8.40 mg g^{-1} and also demonstrates LLP isotherm behavior.[11,44] Given the high costs associated with producing activated alumina,[22] our result suggests that ATAB could potentially be an attractive and cost-effective alternative for fluoride remediation, although a detailed life cycle assessment cost analysis must be performed, and is currently underway in our laboratory.

The observed LLP isotherm behavior is markedly different from the Freundlich isotherms observed in raw[22] and thermally activated bauxites,[23] and suggests that surface adsorption is limited by monomolecular surface coverage and supports chemisorption rather than physisorption as the dominant adsorption phenomenon.[44,46] This distinction highlights that treatment of bauxite with 5 M HCl assists in providing formation of a surface environment primed for chemisorption of fluoride, rather than relying on the dispersive, long-chain electrostatic forces exploited in physisorption phenomena. This, in addition to the increased surface area, could explain why maximum adsorption densities are higher for ATAB when compared to raw bauxite and TAB.

Adsorbent dose is an important parameter when assessing the performance of adsorbents for fluoride removal. Figure 3B
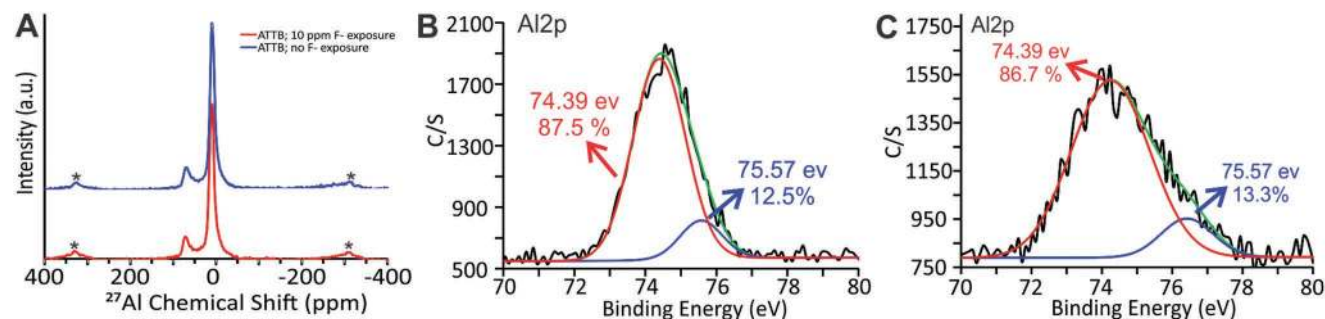
Figure 2. A) ^{27}Al MAS-NMR of ATAB before fluoride adsorption (blue) and after adsorption of fluoride (red); * denotes spinning side bands. High-resolution Al2p XPS spectra of ATAB B) before and C) after exposure to 10 ppm fluoride, showing original (black), composite fit (green), aluminum oxide (blue), and boehmite (red), and corresponding integration percentages.
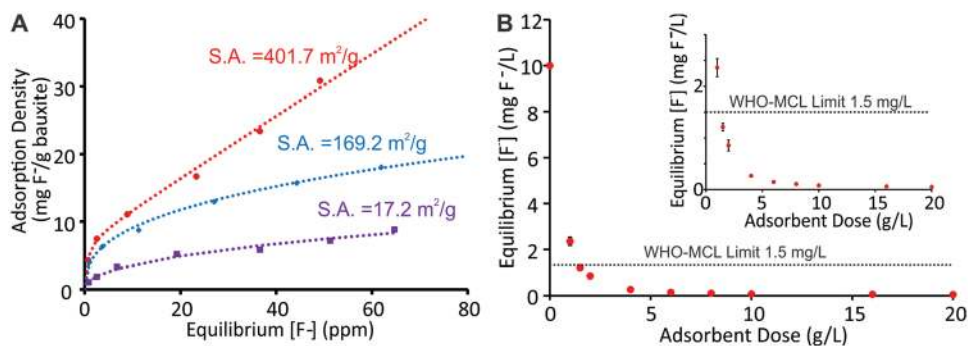
Figure 3. A) Isotherm plots showing equilibrium [F⁻] (ppm) versus adsorption density (mg g⁻¹) for raw bauxite (purple), TAB (blue), and ATAB (red) with Freundlich (purple dots), Freundlich (blue dots), and Langmuir–linear (red dots) isotherms fits, and corresponding surface areas ("S.A.") in respective colors. B) Adsorbent dose (g L⁻¹) versus equilibrium [F⁻] (mg L⁻¹) using ATAB in order to reach fluoride levels below the WHO-MCL limit of 1.5 mg L⁻¹ (black dotted line), with zoomed figure inset (all isotherms and dosage studies using synthetic water adjusted to pH = 6, see the Experimental Section for details).

shows the effect of ATAB dosage on fluoride removal using initial fluoride concentrations of 10 mg L⁻¹. Successive dosage increases from 1 to 20 g L⁻¹ resulting in successive decreases in final fluoride concentration, reaching and then going below the maximum permissible fluoride concentration of 1.5 g L⁻¹. As seen in **Figure 4**B (particularly Figure 3B inset), an ATAB dose of 1.5 g L⁻¹ remediates solutions with initial fluoride of 10 mg F⁻ L⁻¹ to final concentrations of 1.3 mg F⁻ L⁻¹, below the World Health Organization-maximum contaminant level (WHO-MCL) limit. Increasing the ATAB dosage results in lower residual levels of 0.27 and 0.08 mg F⁻ L⁻¹ using doses of 4 and 10 g L⁻¹, respectively. Initially, the residual fluoride concentration decreases sharply with an increase in adsorbent dose (up to 4 g L⁻¹) and thereafter decreases asymptotically toward zero with increasing ATAB dosage up to 20 g L⁻¹.

2.3. Kinetics Study, Effect of Temperature, and Thermodynamic Parameters

Adsorption kinetics represent one of the most important characteristics of adsorbents providing insight about the rate and type of adsorption. The rate of fluoride adsorption using ATAB with initial fluoride concentration of 10 ppm over 24 h at 25, 35, and 50 °C using an adsorbent dose of 1.5 g L⁻¹ (based on dosage studies) is shown in Figure 4A. At temperatures of 25 and 35 °C, the adsorption of fluoride is rapid, remediating fluoride levels to under 1.5 ppm in 40 and 120 min, respectively. Adsorption reaches equilibrium after 300 min and

Table 2. Langmuir–linear partition isotherm values for fluoride adsorption using ATAB with a dosage 1 g L⁻¹.

Isotherm	Equation	Parameters	Value
Langmuir–linear partition	$q = \dfrac{Q_0 b C_i}{1 + b C_i} + k_p C_i$	Q_0 [mg g⁻¹]	7.47
		b [L mg⁻¹]	1.67
		k_p [L mg⁻¹]	4.56E-1
		R^2	0.99

remains steady over the course of the final 19 h. At 50 °C, the adsorption is not as robust, achieving equilibrium fluoride concentrations of 2.4 ppm after 24 h, indicating that temperature has a substantial influence on the performance of ATAB as a fluoride adsorption agent.

The kinetics of fluoride adsorption using ATAB were evaluated pseudo-second-order[47] and intraparticle diffusion[48] models. The pseudo-second-order model was determined as the best fit for all temperatures ($R^2 > 0.99$), and is described by Equation (2)

$$\frac{t}{q_t} = \frac{1}{k_2 q_e^2} + \frac{1}{q_e} t \tag{2}$$

where k_2 is the second-order rate constant for adsorption (g mg⁻¹ min⁻¹), q_t is the amount of fluoride adsorbed by adsorbent at any time (mg g⁻¹), and q_e is the equilibrium fluoride adsorption density (mg g⁻¹). Figure 4B shows the plot of t/q_t versus t yielding a linear relationship ($R^2 > 0.99$ for all temperatures). According to pseudo-second-order kinetics, the rate of adsorption is directly proportional to the number of active sites on the adsorbent surface.[47] This is consistent with the observed LLP isotherm behavior, which specifies that activity is defined by availability of binding sites on the surface of the material. The second-order rate constant, k_2, is calculated to be 6.57×10^{-2}, and the calculated equilibrium adsorption density is 6.08 mg g⁻¹ which is in line with experimentally observed value of 6.20 mg g⁻¹ at 25 °C. A summary of all kinetic parameters is presented below in **Table 3**. Consistent with the observed decreased adsorption density with increasing temperatures, the second-order rate constant also decreases, as temperature is elevated from 25 to 50 °C, from 6.57×10^{-2} to 4.24×10^{-2} g mg⁻¹ min⁻¹.

The possibility of intraparticle diffusion resistance affecting the sorption behavior was explored using the intraparticle diffusion kinetic model,[48] described below by Equation (3)

$$q_t = k_{int} t^{1/2} + C \tag{3}$$

where, t is time, k_{int} is the intraparticle diffusion rate constant (mg g⁻¹ min⁻¹/²), q_t is the adsorption density at t, and C
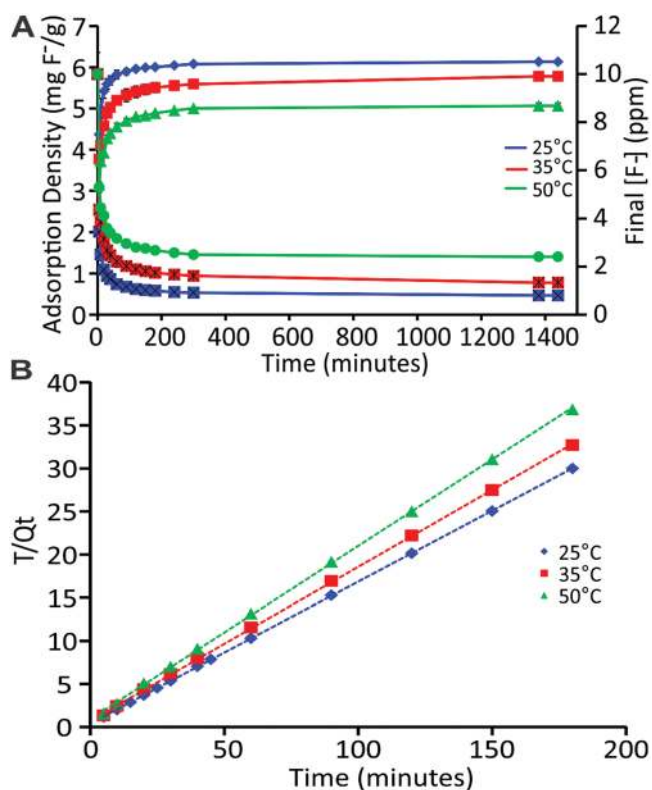
Figure 4. A) Left axis: Plot of adsorption density and final [F-] (right axis) versus time with initial [F-] of 10 ppm for using 1.5 g L^{-1} dosage of ATAB at 25 °C (blue ◊), 35 °C (red □), and 50 °C (green ▲). Right axis: Plot of corresponding change in [F-] versus time at 25 °C (blue), 35 °C (red □), and 50 °C (green ●). B) Pseudo-second order kinetic model plots of time versus T/Q_t at 25 °C (blue ◊), 35 °C (red □), and 50 °C (green ●) for adsorption of fluoride onto ATAB (plot with full time range available in the Supporting Information). All kinetic experiments were performed using synthetic water adjusted to pH = 6, see the Experimental Section for details.
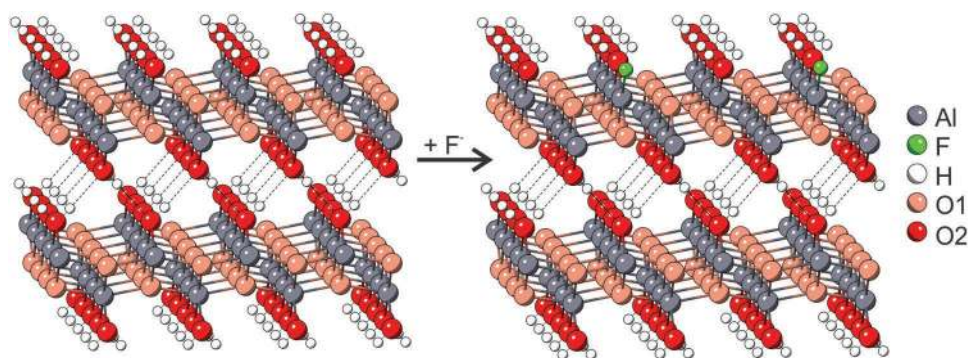
The effect of temperature on fluoride adsorption onto ATAB was studied at 25, 35, and 50 °C for an initial fluoride concentration of 10 ppm, at optimized conditions (pH = 6 and adsorbent dosage of 1.5 g L^{-1}). The related thermodynamic parameters such as $\Delta G°$, $\Delta H°$, and $\Delta S°$ were calculated using the Van't Hoff equation described below by Equation (4) and the equation for free energy, given by Equation (5)

$$\log\left(\frac{q_e}{C_e}\right) = \frac{\Delta S°}{2.303R} - \left(\frac{\Delta H°}{2.303R}\right)\frac{1}{T} \tag{4}$$

$$\Delta G° = \Delta H° - T\Delta S° \tag{5}$$

where q_e is the equilibrium adsorption density, C_e is the equilibrium fluoride concentration, T is temperature, and $\Delta G°$, $\Delta H°$, and $\Delta S°$ are the changes in free energy, enthalpy, and entropy, under standard states, respectively. The thermodynamic parameters were calculated from the plots of $\log(q_e/C_e)$ versus $1/T$ (Figure S8, Supporting Information) to evaluate the thermodynamic feasibility and the spontaneity of the adsorption process. The adsorption process exhibits a $\Delta H°$ of −41.6 kJ mol^{-1} and a $\Delta S°$ of −121.7 J mol^{-1}, resulting in $\Delta G°$ values of −5.02, −3.80, and −1.98 kJ mol^{-1} at 25, 35, and 50 °C, respectively. The negative $\Delta H°$ and $\Delta S°$ values indicate that an exothermic process dominates and overall system entropy decreases. The negative $\Delta G°$ reveals that the adsorption process is spontaneous and exergonic in nature. Increasing temperature from 25 to 50 °C results in $\Delta G°$ values becoming more positive, moving from −5.02 to −1.98 kJ mol^{-1}, respectively, indicating that the favorability of the reaction decreases with increasing temperature, consistent with the nature of exothermic reactions that are entropically unfavorable. The thermodynamic results are consistent with the decrease in adsorption density and decrease in percent fluoride removal observed in kinetics studies.
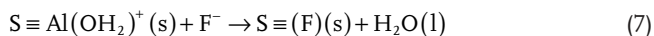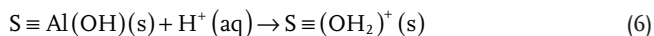
The adsorption of fluoride onto ATAB is useful and potentially industrially relevant given the minimal processing needed to generate it. Of most significance is that the adsorption of fluoride is competitive with the state-of-the-art materials (SOTA) currently employed in industrial fluoride removal, such as activated alumina and calcium dihydroxide (lime).[50] This is significant because lime and activated alumina are highly refined homogeneously pure chemical products that are the consequence of numerous chemical-processing steps incurring significant carbon and monetary cost. This extensive refinement process is inherently cost prohibitive and cumbersome for industrial use, especially considering the large quantities needed for fluoride remediation on an industrial scale. ATAB demonstrates comparable adsorption capacities to the SOTA materials while undergoing only a minimal refinement process— from ore to adsorbent material (two steps)— illustrating the inherent benefit of using ATAB with respect to other adsorbents for fluoride adsorption. The ability of ATAB to competitively perform as an adsorbent extends the boundaries when thinking about how to use natural materials for effective ion adsorption

represents the thickness of the boundary layer.[49] Plotting $t^{1/2}$ versus q_t should yield a linear relationship if diffusion is a dominating rate-determining step, and thus allows for experimental determination of the intraparticle diffusion constant, k_{int}. Figure S7 (Supporting Information) shows the intraparticle diffusion plots for ATAB at 25, 35, and 50 °C. The lack of a linear response suggests that diffusion is not dramatically involved in the mechanism of adsorption of fluoride onto ATAB.

Table 3. Kinetic parameters for fluoride adsorption onto ATAB with initial fluoride concentration of 10 ppm at temperatures of 25, 35, and 50 °C.

Model	Parameter	Initial [F$^-$] [mg F$^-$ L^{-1}] and temperatures [°C]		
		10 ppm F$^-$		
		25 °C	35 °C	50 °C
Pseudo 2nd order	k_2 [g mg^{-1} min^{-1}]	6.57×10^{-2}	4.37×10^{-2}	4.24×10^{-2}
	$q_{e (exp.)}$ [mg g^{-1}]	6.20	5.77	5.06
	$q_{e (calc.)}$ [mg g^{-1}]	6.08	5.60	4.98
	r^2	1.0	0.9998	0.9998
[F$^-$]$_{eq.}$	$C_{eq.}$ [mg F$^-$ L^{-1}]	0.80	1.33	2.40

Scheme 2. (Left) Crystal structure representation of boehmite[51] in its protonated form after treatment with 5 M HCl, and (right) representation after ion exchange with fluoride, resulting in bound fluoride to aluminum center; gray (Al), green (F), white (H), pink (O1), and red (O2).

from contaminated waters, by illustrating that natural material, which undergoes minimal chemical processing, can result in the generation of highly organized frameworks displaying surface areas and porosities generally seen in synthetic materials. Furthermore, this synthetic strategy could be envisaged for numerous other water remediation technologies in the future, such as phosphate and nitrate adsorption.

The mechanism of fluoride removal by ATAB can be described by considering the active site and chemical environment during adsorption. Given that boehmite is the predominant aluminum phase in ATAB, combined with the strong literature precedent showing that fluoride readily exchanges with hydroxyl ions, it is envisaged that a simple ion exchange occurs. During adsorption, the acidic environment imparted though treatment with 5 M HCl facilitates the formation of pseudo-boehmite, or boehmite existing in its protonated state.[29] Adsorption of fluoride would then follow a simple protonation and ligand-exchange mechanism, as shown below in Equations (6) and (7) (where S refers to the ATAB/boehmite substrate)

$$S \equiv Al(OH)(s) + H^+(aq) \rightarrow S \equiv (OH_2)^+(s) \qquad (6)$$

$$S \equiv Al(OH_2)^+(s) + F^- \rightarrow S \equiv (F)(s) + H_2O(l) \qquad (7)$$

The added proton directly to the boehmite substrate makes the adsorbent cationic and facilitates an easier ion exchange with the anionic fluoride, **Scheme 2**.

3. Conclusion

We provide a comprehensive examination of the kinetic and thermodynamic behavior of, as well as examining the active sites in, ATAB which is responsible for the adsorption of fluoride. Adsorption onto ATAB obeys Lagergren 2nd order kinetics signifying that the rate-limiting step of the adsorption mechanism is chemical adsorption, which results in bond formation between adsorbent and adsorbate, in this case the aluminum center of boehmite and the fluoride anion. This determination is supported by intraparticle diffusion studies, which illustrate that diffusive processes are not dominant, and therefore are not involved in the rate-limiting step. The LLP isotherm behavior

shows that adsorption of fluoride onto ATAB is limited by the monomolecular surface coverage. This suggests that a column adsorption process with ATAB may be more effective than the batch processes described herein. One can envisage functionalization of ATAB onto high surface area exposed materials such as steel mesh, which may provide large exposed areas for the requisite monomolecular surface coverage. This may create an environment in which fluoride adsorption onto ATAB can behave optimally. Evaluation of this type of process is currently under way in our laboratory.

The identification of the specific aluminum coordination environments in this study provides a target for additional future processing in order to increase percentage of active fluoride adsorption sites in bauxite. Moreover, future studies such as 2D-correlation ^{27}Al and ^{19}F MAS-NMR are needed to definitively confirm boehmite as the active site in ATAB for the adsorption of fluoride, and are currently underway in our laboratory. Additionally, computational models need to be developed in order to better understand the relationship between BET surface area and the adsorption capability of ATAB. Finally, a detailed life cycle assessment and carbon and cost analysis on the use of ATAB versus activated alumina (produced via the Bayer process) for potential use as an industrial fluoride adsorbent should be performed. This should shed light into the feasibility of implementing ATAB as a potential industrial replacement. Nonetheless, the use of ATAB bauxite for adsorption of fluoride from water shows promising results with maximum adsorption densities comparable to state-of-the-art AA, thus warranting future consideration as primary material choice for adsorption of fluoride from water.

4. Experimental Section

Materials: Hydrochloric acid (37%, ACS reagent) used for acid treatment studies was purchased from Sigma-Aldrich. Deionized (DI) water (>18.2 MΩ) prepared by Millipore (Milli-Q Academic) water purification system was used for all dilutions and batch adsorption studies. NaF (Sigma-Aldrich) was used as fluoride source. 4-morpholineethanesulfonic acid (MES) hydrate (Sigma) was used as a buffer to keep solution pH at 6 ± 0.2. Total ionic strength adjustment buffer (TISAB) was purchased from Sigma-Aldrich.

Preparation of Adsorbent Material: The bauxite used in this study was collected from a mine in Visakhapatnam, Andhra Pradesh, India. It was

dried, ball-milled to a size of 50 μm ± 0.78 (used throughout all isotherm adsorption, kinetic, and dosage experiments), and heated to 300 °C, following procedures reported previously,[23] to obtain TAB. Three grams of TAB was then placed in a 250 mL round bottom flask with a Teflon stir bar, to which 70 mL of 5 M HCl was added. The flask was covered with a septum and placed on a stir plate and stirred at room temperature for 24 h. The solution was removed from stirring, allowed to settle, and then decanted. The resulting material was washed with 200 mL of DI water and vacuum filtered through a glass frit. After filtration, the sample was dried for 2 h at 100 °C to remove excess moisture, and subsequently weighed affording 2.5 g of ATAB (83% mass recovery).

Specific Surface Area, SEM, and XRD Characterization: The specific surface area of newly prepared ATAB was examined with multipoint BET measurements using a Micromeritics Tristar II 3020 instrument. Approximately 0.33 g of ATAB was added to glass tubes and dried overnight in a vacuum at 100 °C and analyzed using N_2 gas sorption. Determination of bulk crystalline mineral composition was obtained from powder XRD patterns obtained using a Bruker diffractometer with a Cu source using a coupled scan with 4 frames at 300 s per frame (θ1 and θ2 ranging from 10,10 to 40,40). XRD peaks for each bauxite sample, processed as 0.1–0.5 g of dry powder, were integrated, merged, and identified using the DIFFRAC.EVA software. A Zeiss Gemini Ultra-55 Analytical Field Scanning Electron Microscope (SEM) was used to obtain high resolution images of ATAB.

X-Ray Photoelectron Spectroscopy Analysis: Two samples of ATAB, fluoride-exposed, and fluoride nonexposed were analyzed by XPS in both vertical (top of surface) and horizontal (cross-section) analysis. After adsorption experiments, ATAB was collected, filtered, and dried for 24 h at 100 °C to remove any excess moisture. The samples were then compressed into pellets using a KBr pellet press. The pellets were then outgassed under vacuum for 24 h. XPS analyses were conducted by the Nanoscale Characterization Facility at the University of Indiana (Bloomington, IN) using a PHI VersaProbe II Scanning X-ray Microprobe system. Band component analysis was performed using MultiPak XPS analysis software, specific for PHI instruments. The binding energies obtained in the XPS analysis were corrected by referencing the C1s line to 284.6 eV. Band fitting was done using a Lorentz–Gauss cross-product function with the minimum number of component bands used for the fitting process, and fitting was undertaken until reproducible results were obtained with correlations of r^2 greater than 0.995.

27Al Magic-Angle Spinning (MAS) NMR Spectroscopy Analysis: ^{27}Al MAS-NMR experiments were conducted using a 14.1T (600 MHz) Bruker Avance III system equipped with a 1.3 mm MAS HX probe that was tuned to 156.35 MHz. The ^{27}Al spectra were externally referenced to the acidic aqueous Al^{3+} cation ($\delta = 0.0$ ppm). Samples were loaded into a zirconia ceramic rotor with Vespel caps and were spun at $v_R = 50$ kHz. The 1D ^{27}Al MAS-NMR experiments were acquired using the standard *zg* experiment, with an RF field of 100 kHz and a recycle delays of 1.0 s over 128 scans.

2D ^{27}Al MQMAS NMR spectra were acquired using the Bruker three-pulse MQMAS experiment with a z-filter (*mp3qzqf*). The RF field for the 3Q excitation pulse was 79 kHz, the 3Q conversion pulse was 179 kHz, and the central-transition selective pulse was 11 kHz. A 20 μs z-filter delay was used with an initial t_1-period of 1 μs, and the phase-sensitive States[43] acquisition mode was used. The resulting 2D data were sheared and processed using TopSpin 3.5, where the shearing routine sets the anisotropic axis parallel with the δ_2 axis.

Isotherm Studies/Fitting: All isotherm experiments were conducted at room temperature 25 °C. Isotherm studies were performed to assess the fluoride adsorption of ATAB. Calibration curves were constructed using standards with fluoride concentrations of 0, 1, 2, 5, 10, 20, 40, 80, and 120 mg L^{-1} in a synthetic groundwater matrix prepared using 50×10^{-3} M MES buffer adjusted to a pH of 6.0 ± 0.2 (in line with our group's previous reports that fluoride adsorption was optimal at pH 6[22,23]), with a constant initial ionic strength of 100×10^{-3} M, using sodium chloride as an electrolyte to balance ionic strength because chloride is known not to influence fluoride adsorption on bauxite.[22]

0.01 g of ATAB was added to polypropylene FALCON tubes containing 10 mL solutions of DI water with either, 0, 5, 10, 20, 40, 60, and 80 ppm

fluoride. Each sample was prepared with a constant initial ionic strength of 100×10^{-3} M using NaCl, and addition of 50×10^{-3} M MES hydrate adjusted to keep solution pH of 6 ± 0.2. Solutions were placed on an analog rotisserie tube rotator and left to mix overnight at 25 °C. Upon completion of stirring, a 2.8 mL aliquot of the slurry was collected in a syringe and filtered through a 25 mm syringe filter with 0.2 μm Nylon membrane before analysis. Filtered aliquots were then mixed with equal volumes of TISABII to complex any free aluminum or iron, and free fluoride was measured using a fluoride ion-selective electrode (Mettler Toledo SevenMulti, perfection). The adsorption density was determined by subtracting the remaining dissolved fluoride concentration from the initial dissolved fluoride concentration and dividing by the mass of adsorbent (vide infra). pH was measured before and after addition of adsorbent, and again after 24 h of mixing. All experiments were completed in triplicate or greater.

Isotherms were modeled using ISOFIT software,[45] which uses a combination of particle swarm optimization and Levenberg–Marquardt nonlinear regression to minimize the weighted sum of squared error. The average across the triplicate experiments as well as the corresponding adsorption density measurement errors were input into the ISOFIT software. Each observation was assigned weighting inversely proportional to its associated measurement error.[52] All isotherms supported by ISOFIT were fitted. The goodness of fit was evaluated using the correlation between measured and fitted observations, the standard deviation of regression, and the corrected Akaike Information Criterion (AICc), as computed by ISOFIT. The AICc is a measure that allows one to compare and rank multiple models and select which best approximates the "true" process. Since the AICc only derives meaning in comparison with the AICc values of other models, the correlation coefficient and standard deviation were additionally used to evaluate overall quality of fit.

Adsorption density, q_e (mg g^{-1}), was calculated using Equation (8), and applied throughout all batch adsorption studies presented in this manuscript

$$q_e = (C_0 - C_e) \times \frac{V}{W_m} \tag{8}$$

where C_0 and C_e are the initial and equilibrium fluoride concentrations (mg L^{-1}), and W_m and V are the adsorbent mass used (g) and the volume (L) of the treated adsorbate solution, respectively.

Minimum Dosage Studies: Minimum dosage experiments were all conducted at room temperature (25 °C). Experiments to determine the minimum bauxite loading needed to remediate an initial fluoride concentration of 10 mg F^- L^{-1} to below the WHO-MCL limit (1.5 mg F^- L^{-1}) were conducted in 10 mL synthetic groundwater solutions in 15 mL to polypropylene FALCON tubes. Synthetic groundwater solutions were prepared with 10 mg F^- L^{-1} (NaF), adjusted to a constant initial ionic strength of 100×10^{-3} M with addition of NaCl, and addition of 50×10^{-3} M MES hydrate adjusted to keep solution pH of 6 ± 0.2. Nine different solutions were prepared with ATAB loadings of 1, 1.5, 2, 4, 6, 8, 10, 16, and 20 g L^{-1}. Solutions were placed on an analog rotisserie tube rotator and left to mix overnight (at least 16 h) at 25 °C. Upon completion of stirring, a 2 mL aliquot of the slurry was collected in a syringe and filtered through a 25 mm syringe filter with 0.2 μm Nylon membrane. Filtered aliquots were then mixed with equal volumes of TISABII to complex any free aluminum or iron, and free fluoride was measured using a fluoride ion-selective electrode (Mettler Toledo SevenMulti, perfection model).

Kinetic Studies: The time-dependent adsorption reactions were conducted over the course of 24 h using a volume of 100 mL in a 250 mL round bottom flask equipped with a Teflon stir bar. Solutions were performed in synthetic groundwater solutions prepared using DI water with addition of 10 or 20 mg F^- L^{-1} (NaF), then brought to an initial ionic strength of 100×10^{-3} M by addition of NaCl, and addition of 50×10^{-3} M MES hydrate adjusted to keep solution pH of 6 ± 0.2. Adsorption experiments were conducted at temperatures of 25, 35, and 50 °C. Solutions were heated by submerging the round bottom flask

into a temperature-controlled water bath, which was monitored with a thermometer over the course of the experiment. An ATAB loading amount of 1.5 g L^{-1} of water was used (in accordance with minimum dosage studies), and the flask was constantly stirred. At desired time intervals, 2 mL aliquots of the slurry was collected in a syringe and filtered through a 25 mm syringe filter with 0.2 μm Nylon membrane before analysis. Filtered aliquots were then mixed with equal volumes of TISABII to complex any free aluminum or iron, and free fluoride was measured using a fluoride ion-selective electrode (Mettler Toledo SevenMulti, perfection).

Supporting Information

Supporting Information is available from the Wiley Online Library or from the author.

Conflict of Interest

The authors declare no conflict of interest.

[1] S. Ayoob, A. K. Gupta, *Crit. Rev. Environ. Sci. Technol.* **2006**, *36*, 433.
[2] T. J. Sorg, *J. – Am. Water Works Assoc.* **1978**, *70*, 105.
[3] S. Jiang, J. Su, S. Yao, Y. Zhang, F. Cao, F. Wang, H. Wang, J. Li, S. Xi, *PLoS One* **2014**, *9*, e96041.
[4] D. L. Ozsvath, *Rev. Environ. Sci. Bio/Technol.* **2009**, *8*, 59.
[5] B. K. Handa, *Groundwater* **1975**, *13*, 275.
[6] S. Jagtap, M. K. Yenkie, N. Labhsetwar, S. Rayalu, *Chem. Rev.* **2012**, *112*, 2454.
[7] J. S. Ahn, *Environ. Geochem. Health* **2012**, *34*, 43.
[8] A. Toyoda, T. Taira, *IEEE Trans. Semicond. Manuf.* **2000**, *13*, 305.
[9] M. G. Sujana, R. S. Thakur, S. B. Rao, *J. Colloid Interface Sci.* **1998**, *206*, 94.
[10] F. Xu, C. Jiang, D. Li, *Sep. Sci. Technol.* **2018**, *53*, 1.
[11] K. K. Yadav, N. Gupta, V. Kumar, S. A. Khan, A. Kumar, *Environ. Int.* **2018**, *111*, 80.
[12] M. Jekel, G. L. Amy, in *Interface Science and Technology*, Vol. *10* (Eds: G. Newcombe, D. Dixon), Elsevier, Cambridge, MA **2006**, pp. 193–206.
[13] L. Samain, A. Jaworski, M. Edén, D. M. Ladd, D.-K. Seo, F. Javier Garcia-Garcia, U. Häussermann, *J. Solid State Chem.* **2014**, *217*, 1.
[14] M. G. Sujana, S. Anand, *Desalination* **2011**, *267*, 222.
[15] N. Das, P. Pattanaik, R. Das, *J. Colloid Interface Sci.* **2005**, *292*, 1.
[16] W.-W. Choi, K. Y. Chen, *J. – Am. Water Works Assoc.* **1979**, *71*, 562.
[17] S. M. I. Sajidu, W. R. L. Masamba, B. Thole, J. F. Mwatseteza, *Int. J. Phys. Sci.* **2008**, *3*, 001.
[18] M. G. Sujana, H. K. Pradhan, S. Anand, *J. Hazard. Mater.* **2009**, *161*, 120.
[19] C. S. Boruff, *Ind. Eng. Chem.* **1934**, *26*, 69.
[20] D. Mohapatra, D. Mishra, S. P. Mishra, G. R. Chaudhury, R. P. Das, *J. Colloid Interface Sci.* **2004**, *275*, 355.
[21] K. H. Peter, *–J. Eng. Appl. Sci.* **2009**, *4*, 240.
[22] K. Cherukumilli, C. Delaire, S. Amrose, A. J. Gadgil, *Environ. Sci. Technol.* **2017**, *51*, 2321.
[23] A. K. K. Cherukumilli, T. Maurer, J. N. Hohman, Y. Mehta, A. J. Gadgil, *Environ. Sci. Technol.* **2018**, *52*, 4711.
[24] H. L. Buckley, N. J. Molla, K. Cherukumilli, K. S. Boden, A. J. Gadgil, *Dev. Eng.* **2018**, *3*, 175.
[25] L. Bray, USGS Mineral Commodities Summaries 2015: Bauxite and Alumina. In Interior, D. o. t., Ed. **2016**.
[26] Organization, W. H., Guidelines for Drinking-Water Quality, in First Addendum to Third Edition, Vol. *1*, **2006**.
[27] J. Fawell, K. Bailey, J. Chilton, E. Dahi, L. Fewtrell, Y. Magara, in *Fluoride in Drinking-Water*, World Health Organization, Geneva **2006**.
[28] M. Authier-Martin, G. Forte, S. Ostap, J. See, *JOM* **2001**, *53*, 36.
[29] Y. Xia, X. Jiao, Y. Liu, D. Chen, L. Zhang, Z. Qin, *J. Phys. Chem. C* **2013**, *117*, 15279.
[30] A. Krause, K. Moroniówna, E. Przybylski, *Z. Anorg. Allg. Chem.* **1934**, *219*, 203.
[31] H. Nitschmann, *Helv. Chim. Acta* **1938**, *21*, 1609.
[32] G. W van Oosterhout, *J. Inorg. Nucl. Chem.* **1967**, *29*, 1235.
[33] K. Bechinê, J. Šubrt, T. Hanslík, V. Zapletal, J. Tláskal, J. Lipka, B. Sedlák, M. Rotter, *Z. Anorg. Allg. Chem.* **1982**, *489*, 186.
[34] K. L. Dubrawski, C. M. van Genuchten, C. Delaire, S. E. Amrose, A. J. Gadgil, M. Mohseni, *Environ. Sci. Technol.* **2015**, *49*, 2171.
[35] G. Busca, *Catal. Today* **2014**, *226*, 2.
[36] C. Morterra, C. Emanuel, G. Cerrato, G. Magnacca, *J. Chem. Soc., Faraday Trans.* **1992**, *88*, 339.
[37] L. Boudriche, R. Calvet, B. Hamdi, H. Balard, *Colloids Surf., A* **2011**, *392*, 45.
[38] M. S. Barrios, L. V. F. González, M. A. V. Rodríguez, J. M. M. Pozas, *Appl. Clay Sci.* **1995**, *10*, 247.
[39] L. F. Nazar, G. Fu, A. D. Bain, *J. Chem. Soc., Chem. Commun.* **1992**, *0*, 251.
[40] P. Paluch, N. Potrzebowska, A. M. Ruppert, M. J. Potrzebowski, *Solid State Nucl. Magn. Reson.* **2017**, *84*, 111.
[41] X. Krokidis, P. Raybaud, A.-E. Gobichon, B. Rebours, P. Euzen, H. Toulhoat, *J. Phys. Chem. B* **2001**, *105*, 5121.

[42] J. T. Kloprogge, L. V. Duong, B. J. Wood, R. L. Frost, *J. Colloid Interface Sci.* **2006**, *296*, 572.

[43] H. Farrah, J. Slavek, W. Pickering, *Soil Res.* **1987**, *25*, 55.

[44] A. Goswami, M. K. Purkait, *Chem. Eng. Res. Des.* **2012**, *90*, 2316.

[45] L. S. Matott, *Isofit Version 1.2*, **2007**.

[46] B. Xing, J. J. Pignatello, B. Gigliotti, *Environ. Sci. Technol.* **1996**, *30*, 2432.

[47] G. Blanchard, M. Maunaye, G. Martin, *Water Res.* **1984**, *18*, 1501.

[48] W. J. Weber, J. C. Morris, *J. Sanit. Eng. Div.* **1963**, *89*, 31.

[49] N. Kannan, M. M. Sundaram, *Dyes Pigm.* **2001**, *51*, 25.

[50] M. Islam, R. K. Patel, *J. Hazard. Mater.* **2007**, *143*, 303.

[51] R. J. Hill, *Clays Clay Miner.* **1981**, *29*, 435.

[52] M. C. Hill, Methods and Guidelines for Effective Model Calibration, with Application to UCODE, A Computer Code for Universal Inverse Modeling, and MODFLOWP, A Computer Code for Inverse Modeling with MODFLOW, **1998**, pp. 98–4005.